
Mid-latitude Cirrus Cloud at the SACOL site: Macrophysical Properties and Large-Scale

Atmospheric State

Jinming Ge¹, Chuang Zheng¹, Hailing Xie¹, Yue Xin¹, Jianping Huang¹, Qiang Fu^{1,2}

¹Key Laboratory for Semi-Arid Climate Change of the Ministry of Education and College of Atmospheric Sciences, Lanzhou University, Lanzhou, 730000, PRC

²Department of Atmospheric Sciences, University of Washington, Seattle, WA, 98105, USA

Corresponding author: Jinming Ge (gejm@lzu.edu.cn)

Key Points:

- Cirrus clouds and their macrophysical properties are derived from two-year ka-band cloud radar observations at the SACOL site.
- The identified cirrus clouds are classified into four distinct regimes and each regime has distinct diurnal and seasonal variations.
- A significant correlation **exists between** cirrus thickness and the vertical velocity.

This article has been accepted for publication and undergone full peer review but has not been through the copyediting, typesetting, pagination and proofreading process which may lead to differences between this version and the Version of Record. Please cite this article as doi: 10.1002/2017JD027724

Abstract

Two-year observations of a Ka-band Zenith Radar at the Semi-Arid Climate and Environment Observatory of Lanzhou University (SACOL) are used to document the midlatitude cirrus cloud macro-properties. Generally, cirrus occurs 41.6% of the observation time and most frequently appear at about 7.2 km above ground level. The cirrus macro-properties are strongly coupled with large-scale atmospheric states, thus its occurrence and location over the SACOL have significant seasonal variations. In addition to the cirrus macro-properties, a k-mean clustering method is used to classify cirrus into four distinct regimes without a prior knowledge about the meteorological process. Contrasting to the different cirrus physical properties in each regime, the cirrus event of each regime has a distinct seasonal distribution and the synoptic conditions from the ERA-Interim reanalysis responsible for each cirrus regime are also quite different. Since global climate models (GCMs) typically overestimate cirrus cloud thickness due to inadequate parameterization or coarse grid resolution, we examined the probability density functions (PDFs) of large-scale vertical velocity associated with each cirrus regime and the relationship between cirrus thickness and vertical velocity. It is found that the differences of the vertical velocity PDFs among the cirrus regimes are as distinct as their macro-properties and a significant correlation exists between cirrus thickness and the vertical velocity, although the large-scale vertical motion is nearly as likely to be descending as ascending when cirrus clouds are observed. This may imply that large-scale vertical velocity can be used to constrain the variations of cirrus thickness simulated by GCM.

1 Introduction

Clouds persistently cover about two-third of the earth [e.g., *Stubenrauch et al.*, 2010] and strongly affect the climate by regulating the incoming solar radiation which reaches at the surface and outgoing longwave radiation (OLR) that radiates to the space through their competing albedo and greenhouse effects [e.g., *Fu et al.*, 2002; *Huang et al.*, 2005; *Li et al.*, 2011; *Liu et al.*, 2013; *Ramanathan et al.*, 1989; *Su et al.*, 2008]. Zelinka and Hartmann [2010] reported that the net down welling radiation of clouds at the top of the atmosphere (TOA) is about -20 Wm^{-2} that is five times larger in absolute value than it caused by a doubling of CO_2 . Due to the large radiative impact of clouds, even subtle changes in cloud coverage, vertical distribution, cloud height, occurrence frequency and optical properties can have dramatic effects on the energy exchange between the atmosphere and the upper and lower boundaries of clouds. This will consequently change the atmospheric heating rate and essentially give rise to a modification in general circulation which in turn largely governs the transport of water vapor and the formation and distribution of clouds [e.g., *Bony et al.*, 2015; *Stephens*, 2005; *Thorsen et al.*, 2013].

Cirrus clouds are composed of large amount of ice crystals and most frequently distribute in the midlatitude storm track regions and the tropics [e.g., *Huang et al.*, 2007; *Wylie and Menzel*, 1999]. They can be formed by synoptic scale motions such as fronts, low pressure systems and jet stream, or mesoscale perturbations for example orographic waves and deep convection etc. [*Sassen et al.*, 2008, and references therein]. Same as water clouds, cirrus clouds can significantly absorb longwave radiation. However, due to their high-altitude location, cirrus clouds radiate thermal radiation at a much lower temperature than the surface,

thus they are like blankets that trap the warm thermal radiation emitted from the underlying atmosphere and the earth's surface, inducing a potentially greenhouse effect on climate. The effective temperature at which the terrestrial thermal energy escapes to space depends on the temperature of the overlying cirrus clouds. The higher of cirrus are located the stronger of its greenhouse effect becomes.

Cirrus clouds have attracted a large amount of scientific awareness for decades [e.g. *Ackerman et al.*, 1988; *Fu*, 1996; *Huang*, 2006; *Luebke et al.*, 2016; *Sassen et al.*, 2008]. Many studies have been done to investigate the mechanisms of cirrus clouds formation, derive their macro- and micro-properties, examine the relationship between weather conditions and cirrus properties, simulate cirrus evolution, life cycle and their effects on precipitation and global energy budget, and discuss a cirrus-related climate engineering idea to mitigate anthropogenic global warming etc. [e.g., *Berry and Mace*, 2013; *Cziczo et al.*, 2013; *Fu et al.*, 2002; *Huang et al.*, 2017; *Huang et al.*, 2006; *Mitchell and Finnegan*, 2009; *Wang and Sassen*, 2002]. However, cirrus clouds are still a great challenge to be accurately represented in global General Circulation Models (GCMs) for the reasons of incomplete knowledge of the physical and dynamical controls of cirrus that are parameterized in GCMs. *Waliser et al.* [2009] have shown that there were large differences in Ice Water Path (IWP) among different climate models, and this difference can be a factor of 6 between the largest and smallest values even when the two largest outliers are removed. *Williams and Webb* [2009] found that models produced cirrus clouds were generally too thick relative to measurements. These large discrepancies of cirrus properties in GCMs will further affect the accurate calculation of cirrus radiative effects and estimation of its response to a climate

change. Thus, cirrus clouds remain the largest source of uncertainty of climate changes prediction.

Long-term continuous measurements are an important step to provide adequate and detailed cloud process observations that are essential for better understanding the relationships between cirrus properties and weather conditions, improving the parametrization of cirrus in GCMs and constraining the models' outputs. Ground-based millimeter-wavelength cloud radar has been recognized as an effective and important tool in characterizing cloud process during the past decades [Kollias *et al.*, 2007]. Because of their short wavelengths, cloud radars have excellent sensitivity to small cloud droplets and ice crystals, and can penetrate clouds with multiple layers from the bottom through the top and acquire detailed cloud vertical structure information with high temporal and spatial resolutions. In July 2013, a new generation of Ka band Zenith Radar (KAZR) was deployed in China at the Semi-Arid Climate and Environment Observatory of Lanzhou University (SACOL) site (latitude: 35.946°N; longitude: 104.137°E; altitude: 1.97 km) [Huang *et al.*, 2008], providing an opportunity to observe and reveal the detailed structure of the mid-latitude clouds over the semi-arid regions of East Asia. In this paper, we firstly investigated the macro-properties of cirrus clouds observed by the KAZR and cluster the cirrus clouds into four different regimes according to their physical properties. Then the large scale atmospheric states for different cloud regimes are examined to reveal the relationship between the cirrus properties and the dynamic and thermodynamic conditions. The KAZR and the large scale atmospheric conditions are described in section 2a. The methods for cirrus identification and clustering are introduced in section 2b and 2c, respectively. The cirrus

macro-properties and the link to the large scale atmospheric state are shown in section 3. Summary and conclusions are given in section 4.

2 Data and Methods

2.1 Data sets

The primary instruments that we used in this study is the KAZR which has been described by Ge et al. [2017]. KAZR is a dual-polarization Doppler radar operated with two modes. One is called a “chirp” mode, because it has a relative long waveform and the frequency changes with time. This waveform is compressed through the use of linear-FM (frequency modulation) and can achieve a radar sensitivity as high as about -68 dBZ at 5 km [Zhu et al., 2017]. This mode is efficient in penetrating low-level clouds and detecting high clouds. The other mode is called “burst”. A short pulse is transmitted at this mode to view clouds as low as 0.2 km above ground level (AGL). The chirp pulse is transmitted at 34.89 GHz while the burst pulse is transmitted at 34.83 GHz. The characteristics of the SACOL KAZR is stable and it has been continuously operated since the radar was set up in July 2013. In this paper, we mainly use two-year radar reflectivity data with a temporal and vertical resolution of 4.27 s and 30 m, spanning from August 1st, 2013 to July 31st, 2015 during which KAZR provides more than 96.8% useful data. The longest system shutdown of five days from July 26th to 31st, 2014 is caused by a high shelter temperature. To determine and count high clouds occurrence and location, the first step is the discrimination of signal from noise (i.e. cloud mask). This process was achieved by using an improved cloud mask algorithm for cloud radar proposed by Ge et al. [2017]. As shown in Fig.1, hydrometeors are well identified from the original observed data by this method.

The 6-hourly daily atmospheric conditions, including horizontal winds, vertical motion, temperature, humidity from the ERA-Interim data, which is the latest global atmospheric reanalysis produced by the European Centre for Medium-Range Weather Forecasts (ECMWF) [Dee *et al.*, 2011], are used to demonstrate the relationships between cirrus cloud properties and large-scale atmospheric state. The temperature data is interpolated to each radar bin through the hydrostatic equation and further used in the cirrus cloud identification process.

2.2 Cirrus clouds identification

Based on the cloud mask results, the KAZR observed clouds are further identified as cirrus by adopting the criteria proposed by Mace *et al.* [2006]. The definition of cirrus in the method requires the temperature of radar echo cloud top to be colder than -30°C , and the temperatures of both the radar maximum dBZ layer and cloud-base to be colder than 0°C . In addition to these minimum temperature requirements, a score of 15 is necessary according an empirical summation formula [Mace *et al.*, 2006]. This additional criterion requires the layers to be considered as cirrus should be somewhat colder than the minimum temperature conditions. The flexible empirical approach can ensure the ice-phase processes are dominant in the clouds without impose any arbitrary constrains on the boundary of the cloud layer, and will also exclude deep convection cloud layers that are capped by cirrus and precipitating cloud systems. After cirrus clouds are identified, the consecutive profiles where contain continuous cirrus clouds will be firstly identified as a cirrus event. Although the cirrus identifying method can largely preserve the contiguous cirrus event from being separated into multiple events[Mace *et al.*, 2006], it is clear in Fig. 1b that a small part of the cloud about 40

minutes around 2200 UTC was not recognized as cirrus. Considering the large scale atmospheric conditions may not change too much within a few hours, we then define that two identified cirrus clouds will be treated as a cirrus event if the time interval between them is less than an hour.

2.3 Clustering of cirrus events

The cirrus events were partitioned into different groups (i.e. cluster) by applying a k-means clustering algorithm [*Jain et al.*, 1999, and references therein] to the mean cloud top height, spanning time and thickness of each cirrus event. The k-mean method classifies all data elements into the predefined k clusters by iteratively searching the cluster centroids until meeting the convergence criterion to maximize the similarity within each cluster [*Gordon and Norris*, 2010]. In order to ensure each data element equally contribute to clustering, the values of cloud top height, spanning time and thickness were normalized to the range from 0 to 1. The similarity is measured by the Euclidean distance. In each cluster, the variance between the vector for the cirrus events and the vector of the cluster centroid is minimized. Since a properly predefined number of cluster is necessary and the convergence results depend on the initial centroids (seeds), we repeated the analysis for an increasing number of k from 3 to 10, and run the cluster analysis 100 times based on different random initial seeds for each k number. Following the logical proposed by Berry and Mace [2013] and Rossow et al. [2005], the optimal k in this study is selected as four, because it is minimum number that: (1) the resulting centroid histogram patterns do not change significantly for different initial seeds, (2) the resulting centroid patterns differ from each other substantially, and (3) the

distance between cluster centroids are larger than the dispersions of the cluster member distances from the centroid. The final cluster set was chose with the least sum of variance around each of the four cluster centroids among the 100 test results.

3 Results

3.1 Mean cirrus properties

A joint radar reflectivity-height histogram with a height bin of 0.5 km and a reflectivity bin of 2 dBZ is built up based on the two-year radar identified cirrus profiles to give an overview of cirrus occurrence as shown in Fig.2a. Generally, the reflectivity of cirrus ranges approximately from -60 to 14 dBZ, most frequently occurring at about 7.2 km associated with a value of -17 dBZ. The radar reflectivity decreases with increasing height. This phenomenon is also observed by both space- and ground-based cloud radars over other regions above freezing level [Liu *et al.*, 2010; Marchand *et al.*, 2009; Protat *et al.*, 2009] which is because larger cloud droplets will be generated in the lower atmosphere due to the higher water content for deposition and aggregation growth in that layer. While, a second mode also can be seen in Fig. 2a at the lower left side of the histogram (i.e. $\text{dBZ} \leq -42, \text{Height} \leq 7 \text{ km}$) where the radar reflectivity increases with increasing height. This mode roughly accounts for 4.7% of the total cirrus data. Interestingly, we found that this part of data is mainly distributed either at the top or the bottom of cloud layers as shown in Fig. 2b. The cloud height is normalized as that cloud base corresponds to 0 and cloud top to 1. We further plot the joint reflectivity-height histogram for the top one-tenth (Fig. 2c) and the bottom 10 percent (Fig. 2d) of all cloud layers to examine if the variation trend shown in the second mode of Fig. 2a is distinct at all cirrus boundary layers. The reflectivity of the maximum frequency at each

height shows an increase with height at the both top and bottom of cirrus layers. This trend for cloud top layer may be explained by the homogeneous ice nucleation mechanism that the number of ice crystals nucleated by homogeneous freezing increases with decreasing temperature (i.e. increasing height). For the cloud base layer, cloud droplets sublimate when they settle through this subsaturated layer. Lower cloud base generally corresponds to higher temperature and lower relative humidity that may increase the sublimation of ice to be smaller particles.

Two-year statistics of cirrus occurrence, which is the ratio of the number of identified cirrus profiles to the total number of available profiles, are shown in Fig. 3. One can see that cirrus occurrence at the SACOL has a significant seasonal variation which is associated closely with the annual variation of the meteorological conditions. Cirrus occurs more often in cold season than warm season over this region. It reaches the maximum occurrence of 60% in March when the subtropical jet stream is relatively strong and cold front occurs most frequently over broad area of northern China. Then the occurrence gradually drops to the minimum about 24% in August (Fig. 3a) when the relative humidity (RH) in the upper tropospheric is much lower than other seasons with relative weak vertical motions. The vertical distribution of cirrus occurrence, which is defined as the number of cirrus in each vertical interval (i.e. 30 m) divided by the total number of observed profiles, exhibits a peak of 22% at about 7.2 km AGL in Fig. 3b. Interestingly, the height of maximum cirrus occurrence in altitude above mean sea level (i.e. about 9.2 km) is almost the same with the eight-year statistic result for the high clouds at the ARM SGP site [*Mace and Benson, 2008*]. The time-height cross section of cirrus occurrence and tropopause that is derived from

ERA-interim data by using a thermal and dynamic blended method proposed by Wilcox et al.[2012] are plotted in Fig. 3c. One can see that cirrus clouds tend to occur at higher altitude in warm season than those in cold season which track the annual cycle of tropopause height. Similar findings that cirrus tops tend to be closer to the tropopause during cold season than warm season and a small fraction of cirrus tops can be above the mean tropopause in spring were also observed over the SGP site reported by Mace et al.[2001].

Since cloud top and base heights can largely influence the cloud radiative effects on thermal infrared radiation at both the surface and the top of the atmosphere, the monthly variations and frequency distributions of radar-echoed cirrus cloud base and top heights are presented in Fig. 4. Similar to the vertical resolved distribution of cirrus occurrence in Fig. 3c, cirrus cloud top and base heights show a strong seasonal trend (Fig. 4a & 4b). Cirrus top height has a minimum median value of 7.1 km AGL in January and exhibits an increase in summer, peaking in August with the monthly median values of 10.0 km AGL, and then gradually decreases as winter approaches which again is apparently limited by the evolution of tropopause. Cirrus base height has the same annual trend as top height, but with a smaller magnitude. The maximum and minimum monthly median values of cirrus base height are 8.5 and 5.1 km AGL, respectively. The maximum occurrence frequencies of the cirrus top and base are 13.7% and 10.6% at 8.0 and 6.5 km AGL, respectively. The annual mean cirrus base height listed in Table 1 is similar as it zonal averaged at the same latitude from A-train satellite observations, however the mean cirrus top height from our radar is about 0.5 km lower than it from CALIPSO [Nazaryan et al., 2008; Sassen et al., 2008] which may be due to the high sensitivity of lidar to small particles. The cloud base and top distributions are

further inspected by examining the joint height-temperature histograms. It is obviously that two modes, existing in Fig. 4e & 4f, show a linear correlation between cirrus top (base) height and temperature with a slope (i.e. lapse rate) of about $8^{\circ}\text{C}/\text{km}$ for the two modes of cirrus base and the lower mode of cirrus top, and $6^{\circ}\text{C}/\text{km}$ for the upper mode of cirrus top. Each mode identified in Fig. 4e & 4f is mainly dominated by the cirrus from a particular season. The mode with relative smaller occurrence frequency in the upper troposphere is mainly derived from warm season (May to October) during which the coldest cirrus occurs, while the mode in the lower troposphere is mostly from the cold season (November to April). It is apparently that cirrus occurs over a broader range of temperature in warm season than it in cold season. Although cirrus top in warm season is generally higher than cold season, the maximum of cirrus top occurrence in warm season appears at a higher temperature comparing with that in cold season.

3.2 Characteristics of cirrus regimes

From the above results, it is clear that cirrus macro-properties have apparent seasonal variations. There is no doubt that the seasonal-dependent cirrus properties are related to the dynamics and thermodynamics of the atmosphere in different seasons. In order to better understand how large-scale atmospheric conditions affect cirrus characteristics, cirrus events are further grouped into 4 distinct cloud regimes based on the clustering analysis which is proved to be an effective method to understand the connections between cloud properties and synoptic processes [Berry and Mace, 2013; Gordon and Norris, 2010; Jakob and Tselioudis, 2003; Zhang *et al.*, 2007].

The four cirrus regimes are physically determined from the cirrus geometric parameters (i.e. cloud top height and thickness) and persistence without a prior knowledge about the meteorological process. The mean values for each of the cirrus regimes are listed in table 1. The four cloud regimes are 1) thick cirrus clouds with a mean thickness of 2.22 km, a moderate mean persistence of 7.5 hours and a cloud top of 8.31 km on average (i.e. C1); 2) upper-troposphere thin cirrus with the smallest thickness and persistence of 0.90 km and 1.5 hours, respectively, and the highest mean top of 9.8 km (AGL) as shown in table 1 for C2; 3) extensively thick cirrus (C3) with the largest thickness of 2.83 km and the longest persistence of 17.7 hours; 4) mid-troposphere thin cirrus clouds (C4) with similar thickness and persistence to C2, but the lowest cloud top at about 6.7 km (AGL).

Fig. 5 shows the joint reflectivity-height histograms for each of the four cirrus regimes. Interestingly, the cirrus radar reflectivity is better correlated with height (i.e. temperature) for the regimes of C1 and C3 comparing with the relationships for C2 and C4. For the thin cirrus regimes shown in Fig. 5b and 5d, the radar reflectivity mainly distributes over a relatively smaller range indicating a smaller cirrus particle size and a narrow distribution than those for thick cirrus regimes, and the reflectivity with the maximum frequencies of occurrence does not shows a decreasing trend with increasing height as clearly shown in Fig. 5a and 5c. Note that the ice water content are usually retrieved through establishing the temperature and reflectivity dependent expressions[Hogan *et al.*, 2006], however Fig. 5 demonstrates that the relationship for different cloud regimes, which corresponds to different synoptic processes, can be quite different and thus it may be difficult to narrow the retrieval uncertainties of cirrus microphysical properties if one parameterization formula is applied for all different

clouds regimes.

To provide an overall picture of the relationship between atmospheric states and cirrus clusters, the seasonal distribution of the event number and the diurnal cycle for each cirrus regime are plotted in Fig. 6 and 7, respectively. Since cloud formation are close coupled to the large-scale circulations, it is not surprising that each cirrus regime has a distinct seasonal evolution. As Fig.6 shown, the number for C1 tends to be uniformly distributed throughout most of the year, except in the transitional months (i.e. March, May, June, September) between seasons when perturbations caused by different weather systems frequently happen inducing a significant increase of its formation. The number of C2 events exhibits evident peaks in the warmest months (July-September) and a sharp drop in the other months that is consistent with the seasonal variation of tropopause height shown in Fig. 3c. C3 has a preference for appearing in spring during which the front and cyclone systems are most active, and a minimum number in summer months. The number of C4 is relatively smaller in summer months and steadily increase on both sides of summer season reaching the maximum in the coldest months from December to January. Figure 7 demonstrates the apparent diurnal variation of occurrence for each cirrus regime with 1-hour and 30-meter temporal and vertical resolution. Cirrus in C1 tends to occur mostly in early morning and peaks around 0500, then decreases to the minimum at about 1800 local time (LT). C3 is mainly concentrated in the same layers between 4-10 km AGL as C1, but maximizes during night and has smaller occurrence during daytime. This variation is similar as the high cloud diurnal cycle in summer season at the ARM SGP site [Zhao *et al.*, 2017]. However, note that C3 at the SACOL site appears more often in cold seasons. The maximum of thin cirrus (i.e. C2 and C4)

is in the morning between 0800 and 0900 LT, and then its occurrence decreases to less than 2% during the afternoon. The diurnal cycles of cirrus boundary height and thickness in each regime are displayed in Fig. 8. Generally, cirrus thickness varies coincidentally with its occurrence. Comparing to the cloud top height, cirrus base has more apparent diurnal cycle which largely determines the daily variation of thickness. Since the cirrus top does not have much diurnal variation, we may infer that net radiative effect of cirrus over the SACOL region mainly depends on its occurrence timing.

3.3 Large-scale atmospheric state

Clouds formation and development can be significantly controlled by dynamic and thermodynamic conditions [Bony *et al.*, 2004; Yuan *et al.*, 2008]. The two variables of vertical velocity and relative humidity have been considered as key parameters for cirrus evolution and residence [Heymsfield and Miloshevich, 1995; Heymsfield *et al.*, 1998; Muhlbauer *et al.*, 2014b; Walcek, 1994]. We first examine the mean values of these two parameters along with the wind speed and direction at 300 hPa level associated with cirrus occurrence for each regime as shown in Fig. 9. For the thick cirrus (i.e. C1 and C3), the maximum RH region with value greater than 70% centers over a broad area of the SACOL. The mean vertical velocity ω for these two regimes over our site is negative indicating ascending motions. Obviously, the large-scale atmospheric conditions corresponding to C1 and C3 are favorable for cloud formation. One can see that high RH region extends over a larger area with much stronger upward motion for C3 comparing with that for C1. In contrast, cirrus grouped in C3 has larger thickness and longer persistence than those in C1 (see in

Table 1). For the thin cirrus (i.e. C2 and C4), the mean RH reduces to about 55% and the mean vertical velocity turns to be positive over the SACOL. The subtropical jet with relatively weak strength moves to the north of the SACOL which will lead to a rapid increase of the tropopause height [*Fu and Lin, 2011*] over this region and thus cause a high location for C2. A flat ridge with its axis situating to the west of the observatory may account for the weak subsidence. The jet stream is strongest for C4 and the SACOL is just located at the left entrance of the jet that will cause an ageostrophic wind toward the left side of the jet axis (looking downwind direction) and consequently lead to the convergence and subsidence over this region. Although the mean larger atmospheric conditions are apparently unfavorable for cloud generation or maintenance, cirrus clouds in C2 and C4 can still account for 14% of the total cirrus occurrence. This finding is similar with the former studies at midlatitudes [*Mace et al., 2006; Muhlbauer et al., 2014a; Sassen and Benson, 2001*]. Vertical motions are organized on different scales, it is worth nothing to find cirrus frequently occurring in the regions with adverse large-scale conditions. Nevertheless, cirrus clouds in C2 and C4, which are in subsidence and insufficient moistures conditions, have much smaller mean thickness and persistence comparing with C1 and C3 that are under favorable conditions.

The detailed histograms of vertical velocity composited by the four cirrus regimes are shown in Fig. 10a. Although these distributions are the same as Mace et al. [2006; 2001] emphasized that the large-scale vertical motion is nearly as likely to be descending as ascending when cirrus clouds are observed, the differences of the distributions of vertical velocity among the cirrus regimes are as distinct as their macro properties. For thick cirrus clouds, the vertical velocity distributes broadly toward negative values and has a wider range

for the extensive thick cirrus, while the distributions have narrow ranges and are slight skewed to positive values for thin cirrus. To further understand the impact of large-scale vertical velocity on cirrus macro properties, we investigated the variations of cirrus thickness, top and base heights with respect to the vertical velocity for each regime. Figure 8b shows the cloud thickness as a function of the ω at 300 hPa. Interestingly, the thickness is consistently decreased with the ω from strongly upward to intensely downward motions for all the cirrus regimes. The correlation coefficients between the cirrus thickness and the vertical velocity are significant at the 95% confidence level with values ranging from -0.67 to -0.95 for the first three cirrus regimes. The correlation coefficient for C4 is -0.49 which does not pass the significant test. The effects of ω on cirrus base and top heights are plotted in Fig. 10c & 10d.

As one can see, for the C1 and C3 cirrus regimes which are under sufficient water vapor conditions, ascending motion will lower the cirrus base height and rise the cloud top. Possible explanations for this phenomenon may be because stronger ascending motion can lift particles to higher altitudes (i.e. increase the cloud top), deepen the supersaturation layer via adiabatic cooling and maintain the growth of ice crystal particles to larger sizes through the water vapor deposition and aggregation processes until they fall out the supersaturated layer. These falling particles with large size will have longer life time before sublimating to small ones that are beyond the radar sensitivity (i.e. low the cloud base). Note that the relative humidity of environment is much lower when thin cirrus occurs, upward motion affects more significantly on cloud top height rather than base for C2 and C4. This finding is crucial, since current general circulation models (GCMs) has difficulties to correctly represent cloud properties, simulated clouds are often too thick and too horizontally uniform relative to

observations [*Gordon et al.*, 2005; *Luo et al.*, 2005; *Williams and Webb*, 2009]. Our results imply that the large scale vertical velocity may be used as an effective parameter to constrain the variation of cirrus macro- and micro-properties.

The vertical profiles of atmospheric conditions (relative humidity, temperature and vertical velocity) as well as the advective forcings (moisture, temperature and vorticity advections) associated with the different cirrus regimes are shown in Fig. 11, providing further examine of the relationship between cirrus properties and atmospheric thermodynamic and dynamic parameters. Generally, the mean cloud properties of each cirrus regime are well confined by the meteorological conditions and dynamic forcings. The mean height of cirrus layer for each cluster is coincident with the peak height of the composited RH profile, while the cirrus thickness and persistence are obviously with respect to the magnitude of RH as depicted in Fig. 11a. C1 and C3 have similar vertical distributions of atmospheric conditions and dynamic forcings, but with different magnitudes. They both have positive moisture advection (Fig. 11b) and ascending motions from 400 to 200 hPa maximizing at 300 hPa (Fig. 11d). Vertical velocity can be largely explained by temperature and vorticity advections. The warm advection (Fig. 11e) and positive vorticity advection (Fig. 11f), which induces a divergence at the level of advection and is increased with height, can directly explain the reasons for upward motion in C1 and C3. The temperature and vorticity advection forcings indicate that these thick cirrus clouds are generated in the regions ahead of a trough and behind of a ridge. For the thin cirrus, C4 has the strongest descending motions as shown in Fig. 11d. The cold advection and large negative vorticity advection demonstrate that these cirrus clouds are in the zone between the back of a trough and the crest of a ridge. Note that

the mean cloud base height of C4 is similar to that of C1 and C3, and the event number distributions of C1, C3 and C4 are also comparable as shown in Fig. 6. We may infer that cirrus in C4 are possibly formed from upstream and advected over the SACOL site. C2 has the largest moisture advection in upper troposphere. This may be especially important for the maintenance of those thin cirrus at high altitude because the relative humidity and vertical motion are obviously unfavorable for the cloud growth conditions. The temperature advection is nearly zero due to the relative small wind speed and weak temperature gradient in the high-pressure region. The negative vorticity advection gradually decreases with height until above 225 hPa, causing a weak downward motion from middle to upper troposphere as depicted in Fig. 11d-11e.

4 Conclusions

Two-year observations from the KAZR at the SACOL are used to demonstrate the statistics of cirrus cloud occurrence, macro-properties and the relationship between large scale atmospheric states and cirrus properties. Cirrus cloud is identified based on the temperatures at cloud base, top and the maximum reflectivity layer using an empirical equation proposed by Mace et al. [2006]. A k-mean cluster method is used to classify cirrus into four distinct regimes with respect to their geometric parameters and persistence. Large-scale atmospheric states from the ERA-Interim reanalysis are composited by the different cirrus regimes to examine the relationship between cirrus properties and the atmospheric conditions. Vorticity and temperature advections, which are associated with the four cirrus groups and can be used to estimate vertical velocity and infer synoptic pattern evolution, are also investigated.

It is found that overall cirrus clouds occur 41.6% of the observation time and most

frequently appear at about 7.2 km AGL associated with a reflectivity of -17 dBZ. Cirrus occurrence and location over the SACOL have significant seasonal variations. The occurrence peaks in March with a value of 60% and then gradually drops to the minimum about 24% in August, while they tend to occur at higher altitude in warm season than those in cold season that track the annual cycle of tropopause height.

Cirrus clouds are classified into four regimes according to their different physical properties. The thick and extensively thick cirrus clouds are the dominant regimes, which occupy 86.1% of the total observed cirrus profiles at the SACOL, and are associated with favorable synoptic conditions (i.e., large relative humidity, mean ascend motion, warm advection and positive vorticity advection) for cloud formation. Thin cirrus can be grouped into high- and mid-troposphere cirrus regimes. These two cirrus regimes are found under adverse environment conditions with mean descending motions, cold advection and negative vorticity advection. In addition to the different cirrus physical properties in each regime, the cirrus event of each regime also has a distinct seasonal and diurnal distributions. The thick cirrus occurs evenly during most of the year, except in the transitional months. The extensively thick cirrus has a preference for appearing associated with front and cyclone in spring. These two dominant cirrus regimes appear more often during night to early morning, we may infer that thick cirrus clouds over the SACOL mainly interact with longwave radiation and thus have significant warming effects. Thin cirrus in upper-troposphere exhibits evident peaks in the warmest months when the subtropical jet move to the north of the SACOL site, while thin cirrus in mid-troposphere is rarely in summer but steadily increase on both sides of summer season. These two thin cirrus regimes peaks in the morning but with an

hour phase difference. The distinct differences of cirrus physical properties, seasonal and diurnal distributions among the four regimes indicate that the cirrus cloud properties significantly depend on large-scale synoptic conditions. Although the PDF of large-scale vertical motion shows that descending motion is as likely as ascending when cirrus clouds are observed, we find a significant correlation between cirrus thickness and the vertical velocity. This implies that large-scale vertical velocity may be used to constrain the variations of cirrus thickness simulated by GCM. Considering cirrus macro-properties is the external appearance of its microphysical structure. We also infer that vertical velocity may have strong effects on cirrus micro-properties. A detailed study on the relationship between vertical velocity and cirrus properties will be carried out in our future work.

Acknowledgments

This work was supported by the National Science Foundation of China (41575016, 41430425, 41521004), China 111 project (No.B 13045), and the Fundamental Research Funds for the Central University (lzujbky-2016-k01). The reanalysis data are from ECMWF Public Datasets center (<http://apps.ecmwf.int/datasets/>). The cirrus properties data will be in the SACOL data archive (<http://climate.lzu.edu.cn>).

References

Boucher, O., et al. (2013), Clouds and aerosols. In: Climate change 2013: The physical science basis, in Contribution of Working Group I to the Fifth Assessment Report of the Intergovernmental Panel on Climate Change, Cambridge Univ. Press, Cambridge, U. K., and New York.

Ackerman, T. P., K. N. Liou, F. P. J. Valero, and L. Pfister (1988), HEATING RATES IN TROPICAL ANVILS, *Journal of the Atmospheric Sciences*, 45(10), 1606-1623, doi:10.1175/1520-0469(1988)045<1606:hrita>2.0.co;2.

Berry, E., and G. G. Mace (2013), Cirrus Cloud Properties and the Large-Scale Meteorological Environment: Relationships Derived from A-Train and NCEP-NCAR Reanalysis Data, *Journal of Applied Meteorology and Climatology*, 52(5), 1253-1276, doi:10.1175/jamc-d-12-0102.1.

Bony, et al. (2015), Clouds, circulation and climate sensitivity, *Nature Geoscience*, 8(4), 261-268, doi:10.1038/ngeo2398.

Bony, S., J. L. Dufresne, H. Le Treut, J. J. Morcrette, and C. Senior (2004), On dynamic and thermodynamic components of cloud changes, *Climate Dynamics*, 22(2-3), 71-86, doi:10.1007/s00382-003-0369-6.

Cziczo, D. J., K. D. Froyd, C. Hoose, E. J. Jensen, M. Diao, M. A. Zondlo, J. B. Smith, C. H. Twohy, and D. M. Murphy (2013), Clarifying the Dominant Sources and Mechanisms of Cirrus Cloud Formation, *Science*, 340(6138), 1320-1324, doi:10.1126/science.1234145.

Dee, D. P., et al. (2011), The ERA-Interim reanalysis: configuration and performance of the data assimilation system, *Quarterly Journal of the Royal Meteorological Society*, 137(656), 553-597, doi:10.1002/qj.828.

Fu, Q. (1996), An accurate parameterization of the solar radiative properties of cirrus clouds for climate models, *Journal of Climate*, 9(9), 2058-2082, doi:10.1175/1520-0442(1996)009<2058:aapots>2.0.co;2.

Fu, Q., M. Baker, and D. L. Hartmann (2002), Tropical cirrus and water vapor: an effective

Earth infrared iris feedback?, *Atmospheric Chemistry and Physics*, 2, 31-37.

Fu, Q., and P. Lin (2011), Poleward Shift of Subtropical Jets Inferred from Satellite-Observed Lower-Stratospheric Temperatures, *Journal of Climate*, 24(21), 5597-5603, doi:10.1175/jcli-d-11-00027.1.

Ge, J. M., Z. Zhu, C. Zheng, H. L. Xie, T. Zhou, J. P. Huang, and Q. Fu (2017), An improved hydrometeor detection method for millimeter-wavelength cloud radar, *Atmospheric Chemistry and Physics*, 17(14), 9035-9047, doi:10.5194/acp-17-9035-2017.

Gordon, N. D., and J. R. Norris (2010), Cluster analysis of midlatitude oceanic cloud regimes: mean properties and temperature sensitivity, *Atmospheric Chemistry and Physics*, 10(13), 6435-6459, doi:10.5194/acp-10-6435-2010.

Gordon, N. D., J. R. Norris, C. P. Weaver, and S. A. Klein (2005), Cluster analysis of cloud regimes and characteristic dynamics of midlatitude synoptic systems in observations and a model, *Journal of Geophysical Research-Atmospheres*, 110(D15), doi:10.1029/2004jd005027.

Heymsfield, A. J., and L. M. Miloshevich (1995), Relative humidity and temperature influences on cirrus formation and evolution: Observations from wave clouds and FIRE II, *Journal of the Atmospheric Sciences*, 52(23), 4302-4326, doi:10.1175/1520-0469(1995)052<4302:rhatio>2.0.co;2.

Heymsfield, A. J., L. M. Miloshevich, C. Twohy, G. Sachse, and S. Oltmans (1998), Upper-tropospheric relative humidity observations and implications for cirrus ice nucleation, *Geophysical Research Letters*, 25(9), 1343-1346, doi:10.1029/98gl01089.

Hogan, R. J., M. P. Mittermaier, and A. J. Illingworth (2006), The retrieval of ice water

content from radar reflectivity factor and temperature and its use in evaluating a mesoscale model, *Journal of Applied Meteorology and Climatology*, 45(2), 301-317, doi:10.1175/jam2340.1.

Huang, J. (2006), Analysis of ice water path retrieval errors over tropical ocean, *Advances in Atmospheric Sciences*, 23(2), 165-180, doi:10.1007/s00376-006-0165-4.

Huang, J., et al. (2017), Dryland climate change: Recent progress and challenges, *Reviews of Geophysics*, 55(3), 719-778, doi:10.1002/2016rg000550.

Huang, J., P. Minnis, B. Lin, Y. H. Yi, T. F. Fan, S. Sun-Mack, and J. K. Ayers (2006), Determination of ice water path in ice-over-water cloud systems using combined MODIS and AMSR-E measurements, *Geophysical Research Letters*, 33(21), doi:10.1029/2006gl027038.

Huang, J. P., J. Ge, and F. Weng (2007), Detection of Asia dust storms using multisensor satellite measurements, *Remote Sensing of Environment*, 110(2), 186-191, doi:10.1016/j.rse.2007.02.022.

Huang, J. P., P. Minnis, B. Lin, Y. H. Yi, M. M. Khaiyer, R. F. Arduini, A. Fan, and G. G. Mace (2005), Advanced retrievals of multilayered cloud properties using multispectral measurements, *Journal of Geophysical Research-Atmospheres*, 110(D15).

Huang, J. P., et al. (2008), An Overview of the Semi-arid Climate and Environment Research Observatory over the Loess Plateau, *Advances in Atmospheric Sciences*, 25(6), 906-921, doi:10.1007/s00376-008-0906-7.

Jain, A. K., M. N. Murty, and P. J. Flynn (1999), Data clustering: A review, *Acm Computing Surveys*, 31(3), 264-323, doi:10.1145/331499.331504.

Jakob, C., and G. Tselioudis (2003), Objective identification of cloud regimes in the Tropical

Western Pacific, *Geophysical Research Letters*, 30(21), doi:10.1029/2003gl018367.

Kollias, E. E. Clothiaux, M. A. Miller, B. A. Albrecht, G. L. Stephens, and T. P. Ackerman (2007), Millimeter-wavelength radars - New frontier in atmospheric cloud and precipitation research, *Bulletin of the American Meteorological Society*, 88(10), 1608-+, doi:10.1175/bams-88-10-1608.

Li, Z., F. Niu, J. Fan, Y. Liu, D. Rosenfeld, and Y. Ding (2011), Long-term impacts of aerosols on the vertical development of clouds and precipitation, *Nature Geoscience*, 4(12), 888-894, doi:10.1038/ngeo1313.

Liu, J., Z. Li, Y. Zheng, J. C. Chiu, F. Zhao, M. Cadetdu, F. Weng, and M. Cribb (2013), Cloud optical and microphysical properties derived from ground-based and satellite sensors over a site in the Yangtze Delta region, *Journal of Geophysical Research-Atmospheres*, 118(16), 9141-9152, doi:10.1002/jgrd.50648.

Liu, Z., R. Marchand, and T. Ackerman (2010), A comparison of observations in the tropical western Pacific from ground-based and satellite millimeter-wavelength cloud radars, *Journal of Geophysical Research-Atmospheres*, 115, doi:10.1029/2009jd013575.

Luebke, A. E., A. Afchine, A. Costa, J.-U. Grooss, J. Meyer, C. Rolf, N. Spelten, L. M. Avallone, D. Baumgardner, and M. Kraemer (2016), The origin of midlatitude ice clouds and the resulting influence on their microphysical properties, *Atmospheric Chemistry and Physics*, 16(9), 5793-5809, doi:10.5194/acp-16-5793-2016.

Luo, Y. L., S. K. Krueger, and S. Moorthi (2005), Cloud properties simulated by a single-column model. Part I: Comparison to cloud radar observations of cirrus clouds, *Journal of the Atmospheric Sciences*, 62(5), 1428-1445, doi:10.1175/jas3425.1.

Mace, S. Benson, and E. Vernon (2006), Cirrus clouds and the large-scale atmospheric state: Relationships revealed by six years of ground-based data, *Journal of Climate*, 19(13), 3257-3278, doi:10.1175/jcli3786.1.

Mace, G., and S. Benson (2008), The vertical structure of cloud occurrence and radiative forcing at the SGP ARM site as revealed by 8 years of continuous data, *Journal of Climate*, 21(11), 2591-2610, doi:10.1175/2007jcli1987.1.

Mace, G. G., E. E. Clothiaux, and T. P. Ackerman (2001), The composite characteristics of cirrus clouds: Bulk properties revealed by one year of continuous cloud radar data, *Journal of Climate*, 14(10), 2185-2203, doi:10.1175/1520-0442(2001)014<2185:tccocc>2.0.co;2.

Marchand, R., J. Haynes, G. G. Mace, T. Ackerman, and G. Stephens (2009), A comparison of simulated cloud radar output from the multiscale modeling framework global climate model with CloudSat cloud radar observations, *Journal of Geophysical Research-Atmospheres*, 114, doi:10.1029/2008jd009790.

Mitchell, D. L., and W. Finnegan (2009), Modification of cirrus clouds to reduce global warming, *Environmental Research Letters*, 4(4), doi:10.1088/1748-9326/4/4/045102.

Muhlbauer, A., T. P. Ackerman, J. M. Comstock, G. S. Diskin, S. M. Evans, R. P. Lawson, and R. T. Marchand (2014a), Impact of large-scale dynamics on the microphysical properties of midlatitude cirrus, *Journal of Geophysical Research-Atmospheres*, 119(7), 3976-3996, doi:10.1002/2013jd020035.

Muhlbauer, A., H. Kalesse, and P. Kollias (2014b), Vertical velocities and turbulence in midlatitude anvil cirrus: A comparison between in situ aircraft measurements and ground-based Doppler cloud radar retrievals, *Geophysical Research Letters*, 41(22),

7814-7821, doi:10.1002/2014gl062279.

Nazaryan, H., M. P. McCormick, and W. P. Menzel (2008), Global characterization of cirrus clouds using CALIPSO data, *Journal of Geophysical Research-Atmospheres*, 113(D16), doi:Artn D16211

10.1029/2007jd009481.

Protat, A., D. Bouniol, J. Delanoe, P. T. May, A. Plana-Fattori, A. Hasson, E. O'Connor, U. Gorsdorf, and A. J. Heymsfield (2009), Assessment of Cloudsat Reflectivity Measurements and Ice Cloud Properties Using Ground-Based and Airborne Cloud Radar Observations, *Journal of Atmospheric and Oceanic Technology*, 26(9), 1717-1741, doi:10.1175/2009jtecha1246.1.

Ramanathan, V., R. D. Cess, E. F. Harrison, P. Minnis, B. R. Barkstrom, E. Ahmad, and D. Hartmann (1989), CLOUD-RADIATIVE FORCING AND CLIMATE - RESULTS FROM THE EARTH RADIATION BUDGET EXPERIMENT, *Science*, 243(4887), 57-63, doi:10.1126/science.243.4887.57.

Rossow, W. B., G. Tselioudis, A. Polak, and C. Jakob (2005), Tropical climate described as a distribution of weather states indicated by distinct mesoscale cloud property mixtures, *Geophysical Research Letters*, 32(21), doi:10.1029/2005gl024584.

Sassen, Z., Wang, and D. Liu (2008), Global distribution of cirrus clouds from CloudSat/Cloud-Aerosol Lidar and Infrared Pathfinder Satellite Observations (CALIPSO) measurements, *Journal of Geophysical Research-Atmospheres*, 113(D20), doi:10.1029/2008jd009972.

Sassen, K., and S. Benson (2001), A midlatitude cirrus cloud climatology from the facility for

atmospheric remote sensing. Part II: Microphysical properties derived from lidar depolarization, *Journal of the Atmospheric Sciences*, 58(15), 2103-2112, doi:10.1175/1520-0469(2001)058<2103:amcccf>2.0.co;2.

Stephens, G. L. (2005), Cloud feedbacks in the climate system: A critical review, *Journal of Climate*, 18(2), 237-273, doi:10.1175/jcli-3243.1.

Stubenrauch, C. J., S. Cros, A. Guignard, and N. Lamquin (2010), A 6-year global cloud climatology from the Atmospheric InfraRed Sounder AIRS and a statistical analysis in synergy with CALIPSO and CloudSat, *Atmospheric Chemistry and Physics*, 10(15), 7197-7214, doi:10.5194/acp-10-7197-2010.

Su, J., J. Huang, Q. Fu, P. Minnis, J. Ge, and J. Bi (2008), Estimation of Asian dust aerosol effect on cloud radiation forcing using Fu-Liou radiative model and CERES measurements, *Atmospheric Chemistry and Physics*, 8(10), 2763-2771.

Thorsen, T. J., Q. Fu, and J. M. Comstock (2013), Cloud effects on radiative heating rate profiles over Darwin using ARM and A-train radar/lidar observations, *Journal of Geophysical Research-Atmospheres*, 118(11), 5637-5654, doi:10.1002/jgrd.50476.

Walcek, C. J. (1994), CLOUD COVER AND ITS RELATIONSHIP TO RELATIVE-HUMIDITY DURING A SPRINGTIME MIDLATITUDE CYCLONE, *Monthly Weather Review*, 122(6), 1021-1035, doi:10.1175/1520-0493(1994)122<1021:ccairt>2.0.co;2.

Waliser, D. E., et al. (2009), Cloud ice: A climate model challenge with signs and expectations of progress, *Journal of Geophysical Research-Atmospheres*, 114, doi:10.1029/2008jd010015.

Wang, Z., and K. Sassen (2002), Cirrus cloud microphysical property retrieval using lidar and

radar measurements. Part II: Midlatitude cirrus microphysical and radiative properties, *Journal of the Atmospheric Sciences*, 59(14), 2291-2302, doi:10.1175/1520-0469(2002)059<2291:ccmpru>2.0.co;2.

Wilcox, L. J., B. J. Hoskins, and K. P. Shine (2012), A global blended tropopause based on ERA data. Part I: Climatology, *Quarterly Journal of the Royal Meteorological Society*, 138(664), 561-575, doi:10.1002/qj.951.

Williams, K. D., and M. J. Webb (2009), A quantitative performance assessment of cloud regimes in climate models, *Climate Dynamics*, 33(1), 141-157, doi:10.1007/s00382-008-0443-1.

Wylie, D. P., and W. P. Menzel (1999), Eight years of high cloud statistics using HIRS, *Journal of Climate*, 12(1), 170-184, doi:10.1175/1520-0442-12.1.170.

Yuan, J., D. L. Hartmann, and R. Wood (2008), Dynamic effects on the tropical cloud radiative forcing and radiation budget, *Journal of Climate*, 21(11), 2337-2351, doi:10.1175/2007jcli1857.1.

Zelinka, M. D., and D. L. Hartmann (2010), Why is longwave cloud feedback positive?, *Journal of Geophysical Research-Atmospheres*, 115, doi:10.1029/2010jd013817.

Zhang, Y. Y., S. Klein, G. G. Mace, and J. Boyle (2007), Cluster analysis of tropical clouds using CloudSat data, *Geophysical Research Letters*, 34(12), doi:10.1029/2007gl029336.

Zhao, W., R. Marchand, and Q. Fu (2017), The diurnal cycle of clouds and precipitation at the ARM SGP site: Cloud radar observations and simulations from the multiscale modeling framework, *Journal of Geophysical Research-Atmospheres*, 122(14), 7519-7536, doi:10.1002/2016jd026353.

Zhu, Z. E., C. Zheng, J. M. Ge, J. P. Huang, and Q. Fu (2017), Cloud macrophysical properties from KAZR at the SACOL (in Chinese) , *Chin. Sci. Bull.*,, doi:10.1360/N972016-00857.

Accepted Article

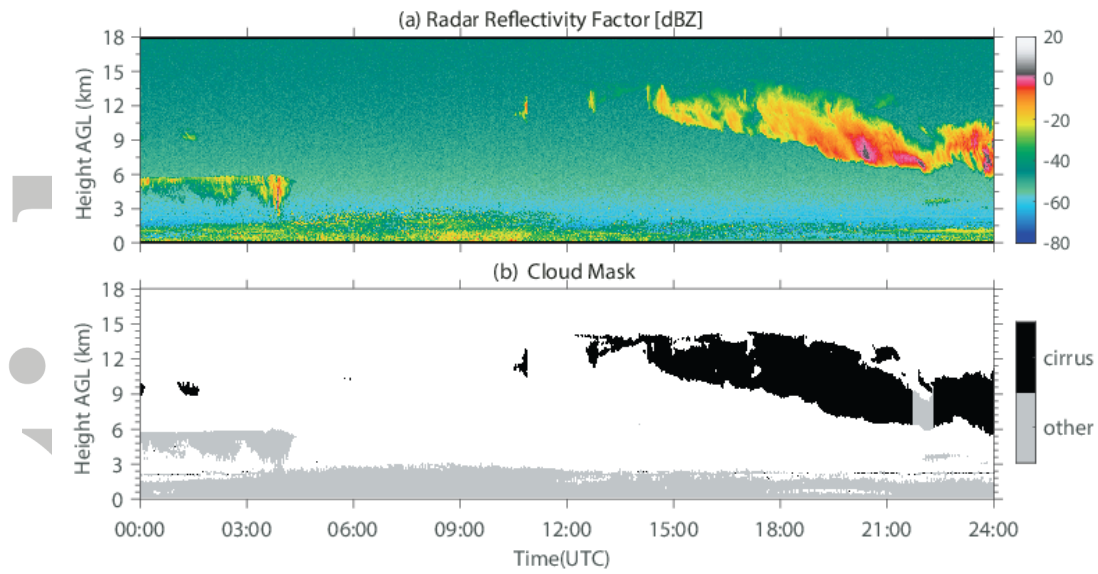


Figure 1. (a) Original radar measured reflectivity factor on June 27, 2015; (b) corresponding cloud mask results. Black color represents the identified cirrus clouds. Gray color is for non-cirrus hydrometeors and clutters.

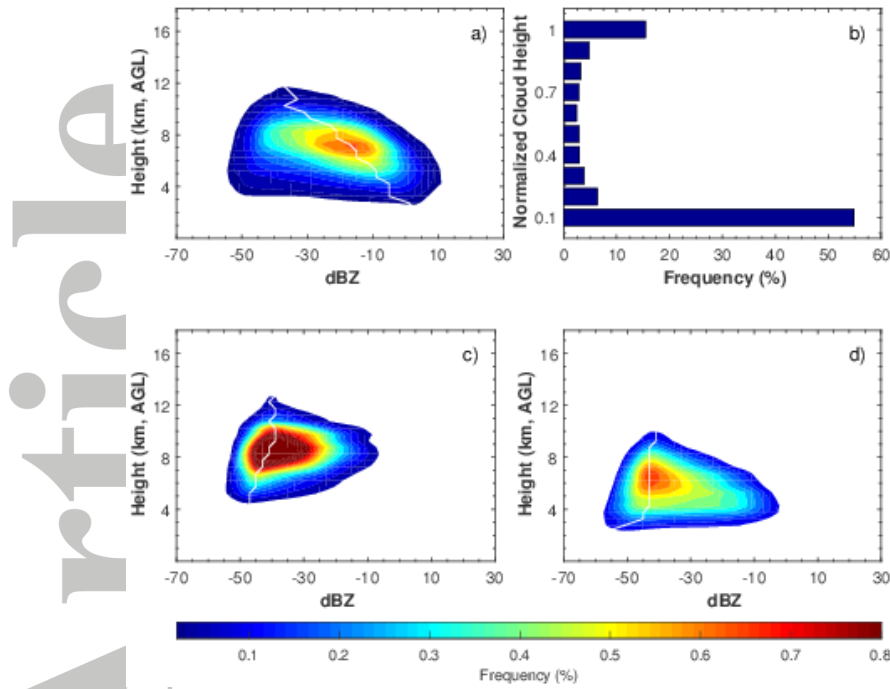


Figure 2. (a) Joint reflectivity-height histogram derived from identified cirrus profiles during August 2013 to July 2015 at the SACOL. (b) Frequency distribution of second mode in Fig. 2a as a function of normalized cloud height. (c) & (d) Joint reflectivity-height histogram for cloud top and base layers, respectively. The white line indicates the reflectivity value with the maximum frequency of occurrence at each height interval.

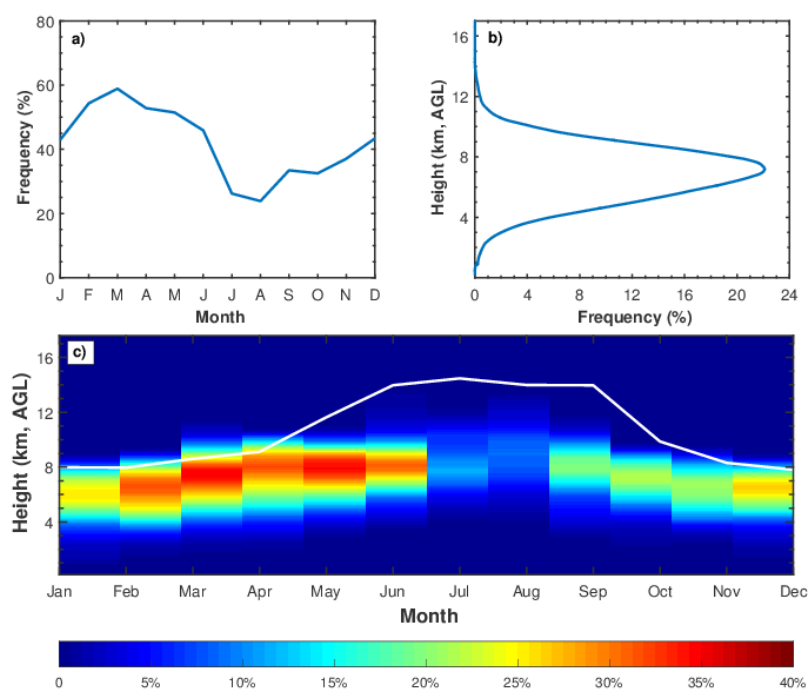


Figure 3. Cirrus occurrence statistics during the study period: (a) Annual cycle of monthly averaged cirrus occurrence. (b) Vertical distribution of cirrus occurrence. (c) Annual cycle of vertical resolved cirrus occurrence. White line represents the monthly averaged tropopause height.

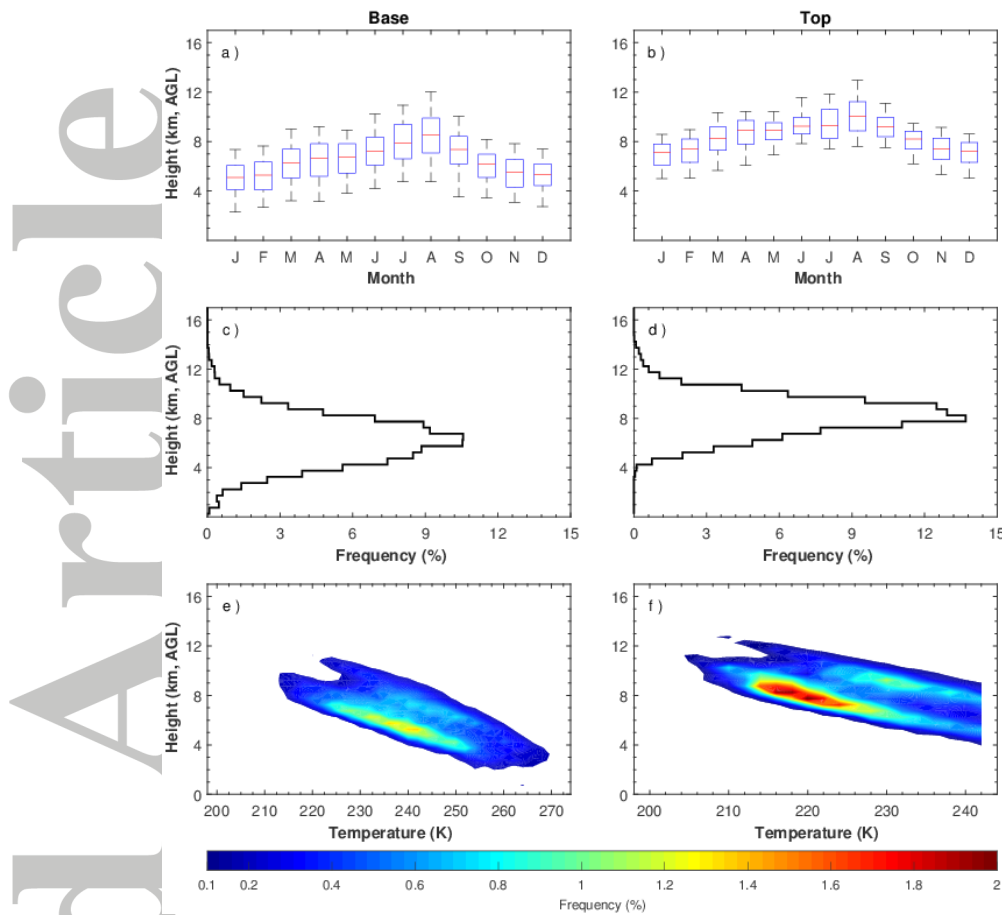


Figure 4. Cirrus cloud top and base statistics: (a) & (b) annual cycle of cloud base and top height. The horizontal line through each box is the median value; the top and bottom of each box marks the 75th and 25th percentiles and whiskers mark the 95th and 5th percentiles, respectively. (c) & (d) Frequency distributions of cirrus base and top height. (e) & (f) Cirrus base and top occurrence frequency as a function of height and temperature, at the SACOL during the study period.

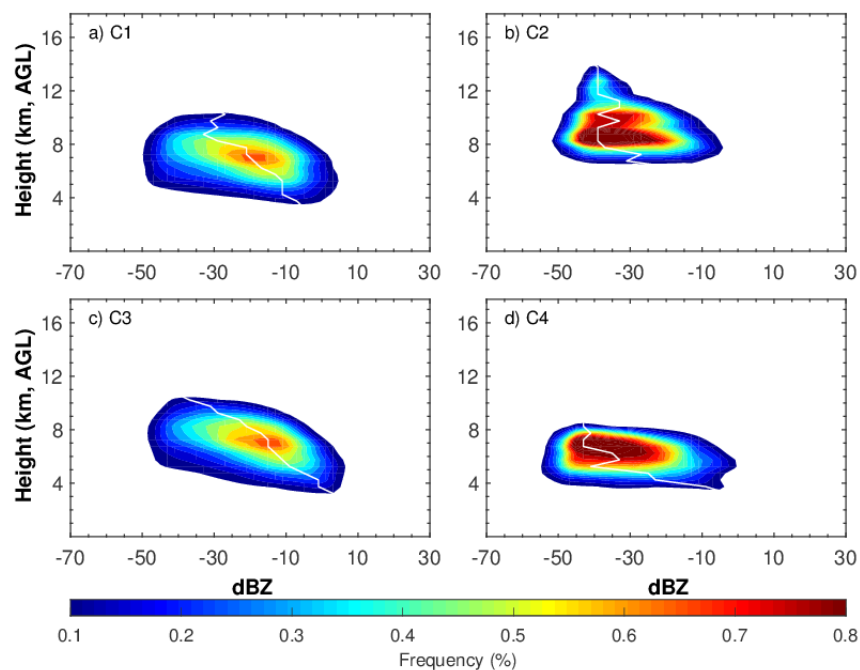


Figure 5. Joint reflectivity-height histograms of the four cloud regimes. The white line indicates the reflectivity value with the maximum frequency of occurrence at each height interval.

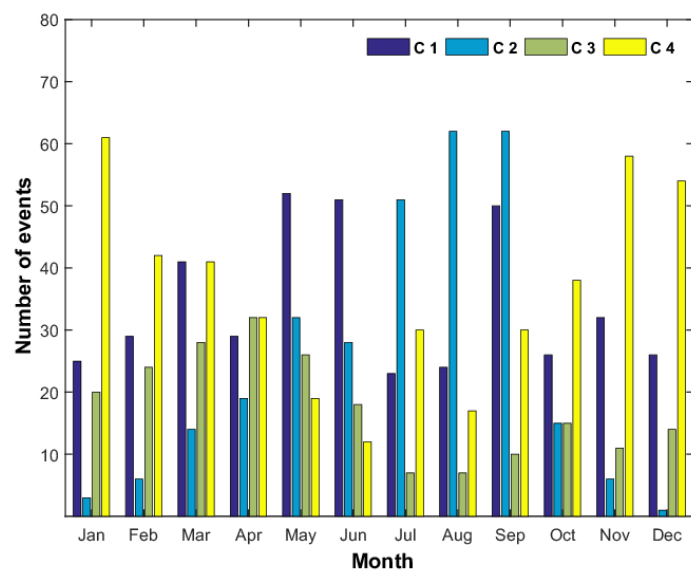


Figure 6. Number of cirrus events for each regime in each month derived from August 2013 to July 2015.

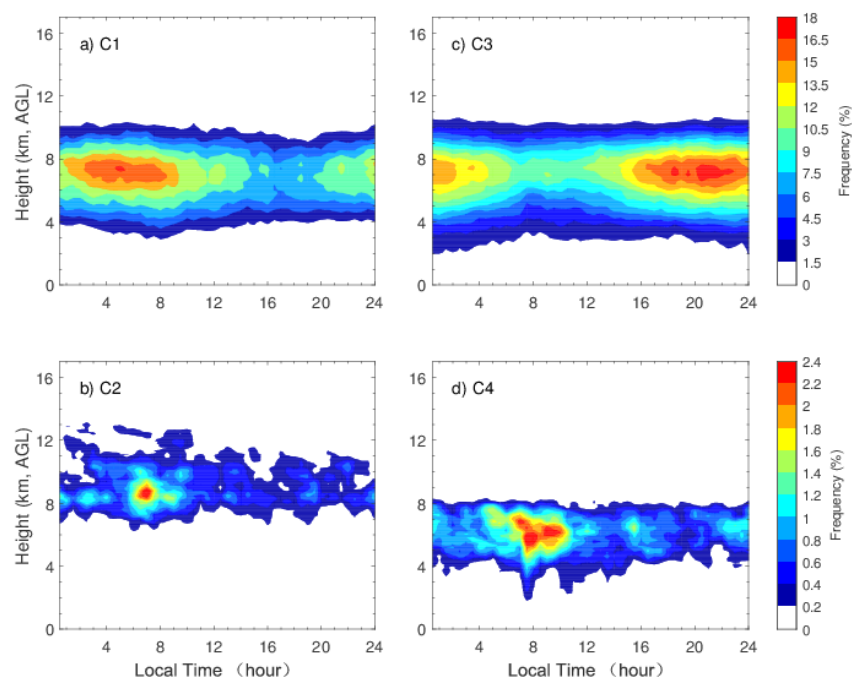


Figure 7. The diurnal cycle of cirrus occurrence for each regime.

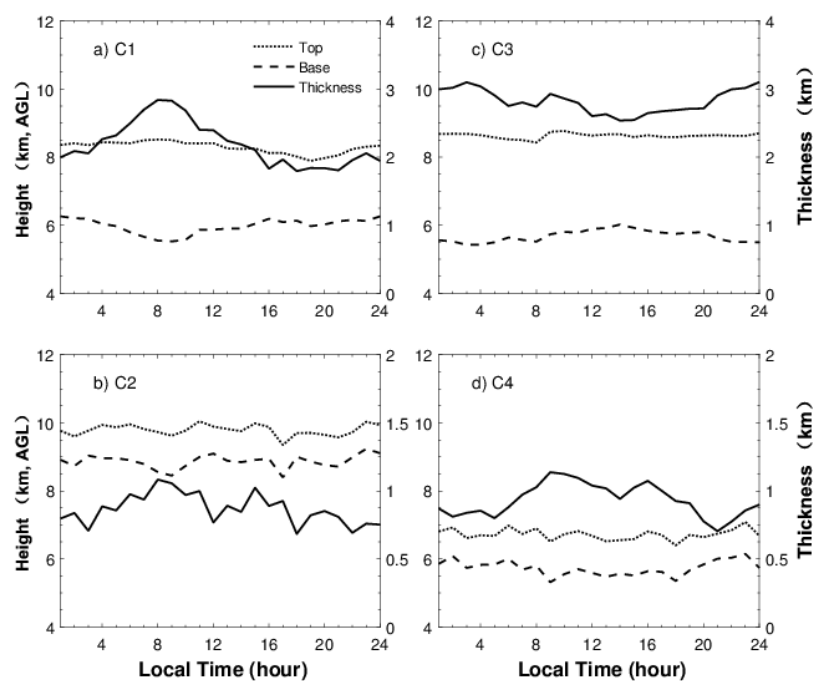


Figure 8. The diurnal cycles of cirrus cloud top and base height, and thickness for each regime.

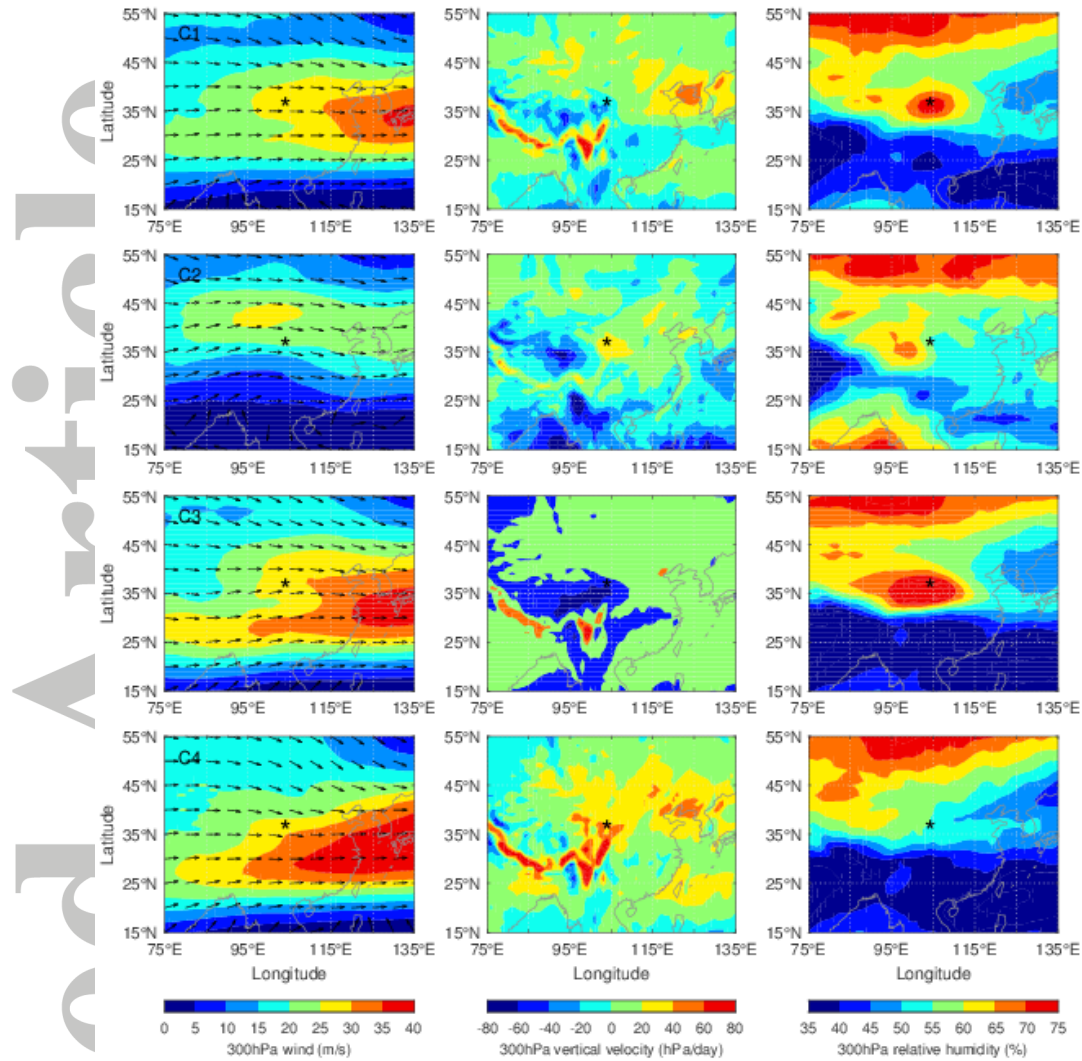


Figure 9. Composite mean wind speed and direction (left panels), vertical velocity (middle panels) and relative humidity (right panels) at 300 hPa from the ERA-Interim reanalysis for the four cloud regimes (i.e. C1 to C4). The asterisk denotes the location of the SACOL site.

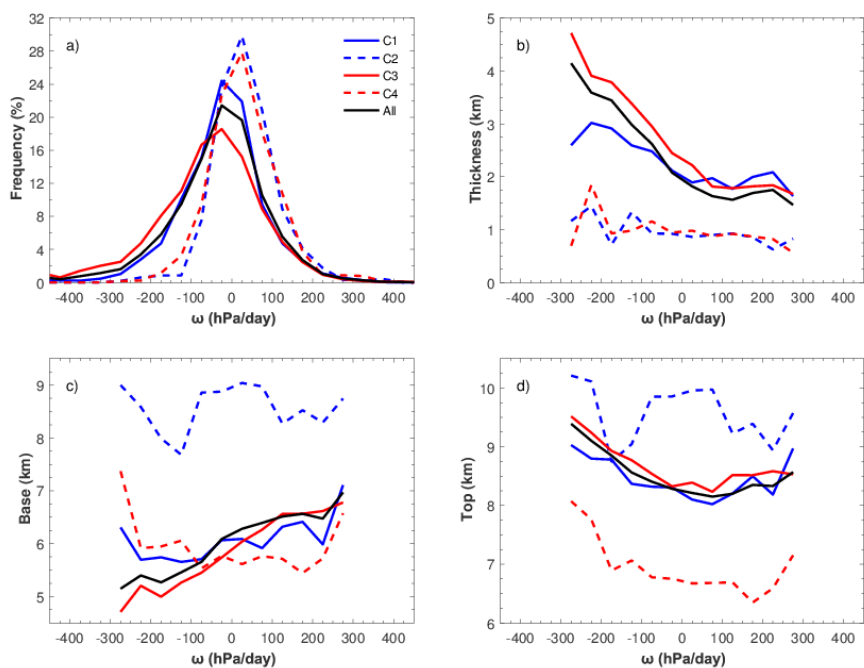


Figure 10. Large-scale vertical motion at 300 hPa from the ERA-Interim reanalysis over the

SACOL when cirrus is observed and mean relationships between cirrus macrophysical properties and vertical velocity. (a) Frequency distribution of vertical velocity. (b)~(d)

Averaged cirrus thickness, top and base heights as a function of vertical velocity. The black lines are for all cirrus. The red and blue lines are for each cluster.

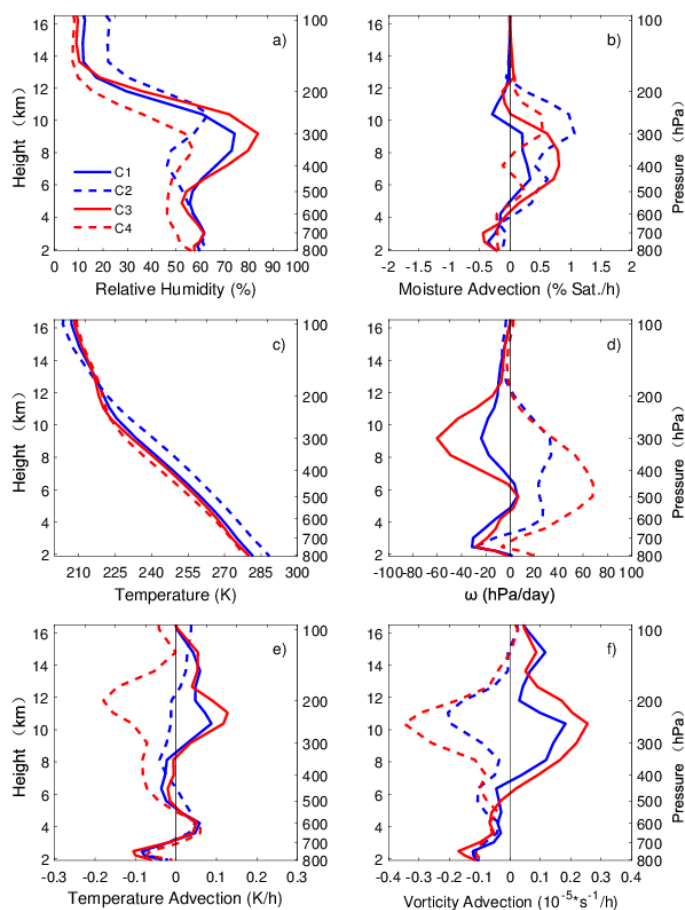


Figure 11. Vertical profiles of mean atmospheric states and advective forcings associated with different cirrus regimes. (a)relative humidity, (b)moisture advection, (c)temperature, (d)vertical velocity, (e)temperature advection, (f)vorticity advection.

Table 1. Mean and standard deviation of cirrus properties for each cluster.

	All Clouds	Cluster 1	Cluster 2	Cluster 3	Cluster 4
Cloud Frequency (%)	41.6	15.9	2.5	19.9	3.3
Top (km, AGL)	8.43±1.48	8.31±1.47	9.80±1.39	8.63±1.29	6.72±1.01
Base (km, AGL)	5.97±1.87	5.97±1.76	8.84±1.49	5.67±1.78	5.71±1.21
Thickness (km)	2.33±1.65	2.22±1.41	0.90±0.67	2.83±1.76	0.95±0.71
Top Temperature (K)	226.3±9.4	228.2±8.8	227.4±9.8	223.4±9.1	231.0±8.5
Base Temperature (K)	234.6±12.6	235.2±11.7	229.7±10.8	235.0±13.7	234.2±10.4
Temperature of Max dBZ (K)	234.2±11.0	235.0±10.4	228.9±9.6	234.2±11.9	234.0±8.3
Persistence (hour)	5.8±6.3	7.5±3.2	1.5±1.8	17.7±3.8	1.5±1.8